Progress In Electromagnetics Research B, Vol. 49, 215–234, 2013

DATA-DRIVEN POLINSAR UNSUPERVISED CLASSIFICATION USING ADAPTIVE MODEL-BASED DECOMPOSITION AND SHANNON ENTROPY CHARACTERIZATION

Hui Song[1], Wen Yang[1, 2, *], Xin Xu[1], and Mingsheng Liao[2]

[1]School of Electronic Information, Wuhan University, Luo-jia-shan, Wuchang, Wuhan 430072, China

[2]The State Key Laboratory LIESMARS, Wuhan University, 129 Luoyu Road, Wuhan 430079, China

Abstract—We introduce a data-driven unsupervised classification algorithm that uses polarimetric and interferometric synthetic aperture radar (PolInSAR) data. The proposed algorithm uses a classification method that preserves scattering characteristics. Our contribution is twofold. First, the method applies adaptive model-based decomposition (AMD) to represent the scattering mechanism, which overcomes the flaws introduced by Freeman decomposition. Second, a new class initialization scheme using a histogram clustering algorithm based on a Dirichlet process mixture model is applied to automatically determine the number of clusters and effectively initialize the classes. Therefore, our algorithm is data-driven. In the first step, the Shannon entropy characteristics of the PolInSAR data are extracted and used to calculate the local histogram features. After applying AMD, pixels are divided into three canonical scattering categories according to their dominant scattering mechanism. The histogram clustering algorithm is applied to each scattering category to obtain the number of classes and initialize them. The iterative Wishart classifier is applied to refine the classification results. Experimental results for E-SAR L-band PolInSAR images from the German Aerospace Center demonstrate the effectiveness of the proposed algorithm.

Received 23 January 2013, Accepted 22 February 2013, Scheduled 22 February 2013

* Corresponding author: Wen Yang (yangwen@whu.edu.cn).

1. INTRODUCTION

As a fast and efficient method for information extraction and scene interpretation, unsupervised classification is of great importance in processing of polarimetric and polarimetric interferometric aperture radar (PolSAR and PolInSAR) data. Among the unsupervised classification algorithms in the literature for PolSAR data, earlier approaches mainly utilized the statistical characteristics of the data [1–4]. For covariance or coherency matrices of multi-look data, Lee et al. [2] derived a distance measure based on the complex Wishart distribution [5] and this distance measure has been incorporated in other classification algorithms. Alternative approaches used the inherent characteristics of PolSAR data and classification based on physical mechanisms [6–8]. Van Zyl [9] proposed classification of terrain types as odd bounce, even bounce and diffuse scattering. For PolInSAR data, classification algorithms are commonly built on PolSAR classification results and the interferometric information is used for further analysis [10, 11]. These methods identified canonical scattering mechanisms based on the target decomposition theory proposed by Cloude and Pottier [12]. In 2004, Lee et al. [13] proposed a new robust classification algorithm based on Freeman decomposition [14]. This method has better stability in convergence and preserves the homogeneous scattering mechanism of each class. Methods that preserve the scattering mechanism have the advantage of providing information for class type identification. An improved algorithm was proposed by Yang et al. [15] that initially divides pixels into seven categories by introducing scattering power entropy and anisotropy parameters.

The Freeman-Durden algorithm has been widely used because of its simplicity and stability, but it has several limitations. As pointed out by Van Zyl et al. [16], a major limitation is that the volume scattering terms all assume the scattering reflection symmetry for the observations. Furthermore, the decomposition may result in many pixels with a negative power. Arii et al. [17] suggested an adaptive model-based decomposition (AMD) technique in which no reflection symmetry is required. We use this decomposition in our classification algorithm instead of Freeman decomposition to overcome the flaws introduced by their assumptions. In addition, determination of the number of classes is also a challenging task for unsupervised classification. Although the proper number can be specified artificially by some experts, an adaptive decision is appealing. The number of clusters poses a model order selection problem. Orbanz and Buhmann [18] considered a Dirichlet process mixture model (DPM)

for image segmentation using a histogram clustering method combined with Markov random fields. The DPM model provides a Bayesian framework for clustering problems with an unknown number of groups.

In this paper, we introduce a data-driven unsupervised classification algorithm that preserves the homogeneous scattering mechanism and determines the number of clusters automatically. The proposed algorithm first calculates the Shannon entropy characteristics of the PolInSAR data and uses three Shannon entropy terms as multichannel data to extract local histogram features, which are the basic inputs for the histogram clustering procedure based on the DPM model. Shannon entropy characterization [19] of PolInSAR data was introduced by Morio et al. [20] and can be decomposed into sums of intensity, polarimetric and interferometric contributions. The three terms are comparable with each other as they are expressed with the same "*unit*". Then the pixels are divided into three canonical scattering categories: surface, volume, and double-bounce scattering by applying AMD. We use the same strategy as [13] to preserve the purity of the scattering characteristics for each class. To each category we apply the histogram clustering algorithm based on the DPM model using histogram features extracted in the previous step. Then the number of clusters is automatically determined and the classes are effectively initialized. In the next step, iterative clustering based on the Wishart distance measure is applied to the three categories to refine the result. Finally, the automated color rendering scheme proposed in [13] is applied for visual evaluation of the classification result.

The remainder of the paper is organized as follows. In Section 2, the basic PolSAR and PolInSAR models, AMD, Shannon entropy characterization, and the DPM model are briefly introduced as the basic theory underpinning this paper. The proposed classification algorithm is described in Section 3. In Section 4, experimental results are presented and analyzed. Conclusions are drawn in Section 5.

2. THEORY

2.1. Basic Models of PolSAR and PolInSAR Data

For PolSAR data, the three unique elements of the scattering matrix can be defined as a complex vector

$$k = \left[S_{hh}, \sqrt{2}S_{hv}, S_{vv}\right]^T, \tag{1}$$

where the superscript T denotes the matrix transpose. For multilook-processed SAR images, the data can be represented by a polarimetric

covariance matrix

$$Z = \frac{1}{n}\sum_{i=1}^{n} k(i)k(i)^{*T}, \tag{2}$$

where $k(i)$ denotes the scattering vector of the ith sample, the superscript * denotes the complex conjugate, and n is the number of looks. Multilook data can be expressed in the form of a polarimetric covariance matrix with a complex Wishart distribution [5]. Let $V = E[Z]$. The probability density function for the covariance matrix is

$$\begin{aligned} p_T^{(n)}(Z) &= \frac{n^{qn}|Z|^{n-q}\exp[-nTr(V^{-1}Z)]}{K(n,q)|V|^n} \\ K(n,q) &= \pi^{(1/2)q(q-1)}\Gamma(n)\ldots\Gamma(n-q+1), \end{aligned} \tag{3}$$

where $q = 3$ for the reciprocal case and $q = 4$ for the biostatic case. Tr is the trace of a matrix, n the number of looks, K a normalization factor, and $\Gamma(\cdot)$ the gamma function. From this probability density function it is possible to define a Bayes maximum likelihood (ML) classifier [2] that assigns the coherency matrix of a pixel of the SAR image to class X_m if $d(Z, X_m) \leq d(Z, X_j)\ \forall j \neq m$, with

$$d(Z, V_m) = \ln|V_m| + Tr(V_m^{-1}Z), \tag{4}$$

where V_m is the mean covariance matrix for the class X_m.

In the case of PolInSAR data, the backscattered signal can be described by a six-element complex target vector corresponding to the polarimetric performances at the two antennae:

$$K = [S_{1hh}, S_{1hh}, \sqrt{2}S_{1hv}, S_{2hh}, S_{2vv}, \sqrt{2}S_{2hv}]^T = [k_1, k_2]^T. \tag{5}$$

The PolInSAR homogeneous region is statically characterized by a 6×6 covariance matrix [20]:

$$\Upsilon = \begin{bmatrix} \langle k_1 k_1^* \rangle & \langle k_1 k_2^* \rangle \\ \langle k_2 k_1^* \rangle & \langle k_2 k_2^* \rangle \end{bmatrix} = \begin{bmatrix} \Gamma_1 & \Omega_{12} \\ \Omega_{12}^* & \Gamma_2 \end{bmatrix}, \tag{6}$$

where $\langle\cdot\rangle$ denotes statistical averaging. Matrices Γ_1 and Γ_2 correspond to the polarimetric measurements at each of the two antennae. Ω_{12} depends on both polarimetric and interferometric characteristics. The covariance matrix Υ also meets the complex Wishart distribution but with $q = 6$ and we can also define an ML classifier similarly.

2.2. AMD for Polarimetric SAR Data

Unlike the well-known three-component decomposition method [14], which may not satisfy the fundamental energy conservation law,

the AMD extended from the non-negative eigenvalue decomposition (*NNED*) model proposed in [16] maintains correctness from a physical point of view. Moreover, the adaptive decomposition technique goes one step further for modification of the covariance matrix of the volume (canopy) component by characterizing it with a mean orientation angle and a degree of randomness. This decomposition model [17] can be written as

$$\langle [C] \rangle = f_v \langle [C_{vol}(\theta_0, \sigma)] \rangle + f_d [C_{double}] + f_s [C_{surface}] + [C_{remainder}]. \quad (7)$$

where $\langle [C_{vol}(\theta_0, \sigma)] \rangle$, $[C_{double}]$ and $[C_{surface}]$ represent the matrices for volume, double-bounce, and surface scattering, and the last term $[C_{remainder}]$ may include additional cross-polarized power that could represent terrain effects and rough surface scattering [16]. As developed in [17], the volume component covariance matrix becomes

$$\langle [C_{vol}(\theta_0, \sigma)] \rangle = [C_\alpha] + p(\sigma)[C_\beta] + q(\sigma)[C_\gamma] \quad (8)$$

where

$$\begin{aligned}
[C_\alpha] &= \frac{1}{8} \begin{bmatrix} 3 & 0 & 1 \\ 0 & 2 & 0 \\ 1 & 0 & 3 \end{bmatrix} \\
[C_\beta(2\theta_0)] &= \frac{1}{8} \begin{bmatrix} -2\cos 2\theta_0 & \sqrt{2}\sin 2\theta_0 & 0 \\ \sqrt{2}\sin 2\theta_0 & 0 & \sqrt{2}\sin 2\theta_0 \\ 0 & \sqrt{2}\sin 2\theta_0 & 2\cos 2\theta_0 \end{bmatrix} \\
[C_\gamma(4\theta_0)] &= \frac{1}{8} \begin{bmatrix} \cos 4\theta_0 & -\sqrt{2}\sin 4\theta_0 & -\cos 4\theta_0 \\ -\sqrt{2}\sin 4\theta_0 & -2\cos 4\theta_0 & \sqrt{2}\sin 4\theta_0 \\ -\cos 4\theta_0 & \sqrt{2}\sin 4\theta_0 & \cos 4\theta_0 \end{bmatrix}
\end{aligned} \quad (9)$$

and

$$\begin{aligned}
p(\sigma) =& 2.0806\sigma^6 - 6.3350\sigma^5 + 6.3864\sigma^4 \\
& - 0.4431\sigma^3 - 3.9638\sigma^2 - 0.0008\sigma + 2.000 \\
q(\sigma) =& 9.0166\sigma^6 - 18.7790\sigma^5 + 4.9590\sigma^4 \\
& + 14.5629\sigma^3 - 10.8034\sigma^2 + 0.1902\sigma + 1.000.
\end{aligned} \quad (10)$$

According to the derivation in [17], the mean orientation angle θ_0 varies from 0 to π and the degree of randomness σ from 0 to 0.91.

We conduct adaptive decomposition according to the following procedure:

(1) For each pixel, the remainder terms matrix is defined as

$$[C'_{remainder}] = \langle [C] \rangle - f_v \langle [C_{vol}(\theta_0, \sigma)] \rangle . \quad (11)$$

We numerically calculate the eigenvalues of $[C'_{remainder}]$ at special θ_0 and σ by varying f_v, and the maximum f_v for which all three eigenvalues of $[C'_{remainder}]$ are non-negative is selected.

(2) After subtracting the resulting volume component, eigenvalue decomposition as proposed by van Zyl [21] is implemented to determine the remaining unknown parameters f_d, f_s and $[C'_{remainder}]$ simultaneously.
(3) By varying θ_0 and σ within the entire range, the parameter set that minimizes the power associated with the remainder matrix $[C'_{remainder}]$ is selected, and then the corresponding power P_v of the pixel is determined.
(4) The covariance matrix described in the three-component scattering approach [14] for C_{double} and $C_{surface}$ is used to determine P_d and P_s.
(5) Repeat steps (1)–(4) for each pixel in the image.

2.3. Shannon Entropy Characterization

For a six-dimensional complex-valued random vector $\vec{K}$ with probability density function $P_\Upsilon(\vec{K})$, Shannon entropy is defined as

$$S\left[P_\Upsilon\left(\vec{K}\right)\right] = -\int P_\Upsilon\left(\vec{K}\right)\log\left[P_\Upsilon\left(\vec{K}\right)\right]d\vec{K}, \tag{12}$$

where $\int\cdot d\vec{K}$ denotes complex six-dimensional integration and $P_\Upsilon(\vec{K})$ follows a six-dimensional Gaussian distribution. The Shannon entropy characterization [20, 22] can be written as

$$S\left[\Upsilon\right] = \log\left\{\pi^6 e^6 \det\left[\Upsilon\right]\right\}. \tag{13}$$

In a homogeneous region of PolInSAR data, the Shannon entropy expression $S[\Upsilon]$ can be decomposed into a sum of three terms:

$$\begin{aligned} S\left[\Upsilon\right] &= S_I\left[\Upsilon\right] + S_P\left[\Upsilon\right] + S_\mu\left[\Upsilon\right] \\ S_I\left[\Upsilon\right] &= 3\log\left(\frac{e\pi I_1}{3}\right) + 3\log\left(\frac{e\pi I_2}{3}\right) \\ S_\mu\left[\Upsilon\right] &= \log\left\{\left(1-\mu_1^2\right)\left(1-\mu_2^2\right)\left(1-\mu_3^2\right)\right\} \\ S_P\left[\Upsilon\right] &= 3\log\left[1-\rho_1^2\right] + 3\log\left[1-\rho_2^2\right]. \end{aligned} \tag{14}$$

The first term represents the intensity contribution and depends on the intensities I_1 and I_2 received by the two antennae. The second term represents the polarimetric contribution and depends on the Barakat degrees of polarization ρ_1 and ρ_2 for the scattering matrices. The last term represents the interferometric contribution and only depends on μ_1, μ_2 and μ_3, the three singular values of the normalized mutual coherence matrix M defined as [20, 23]

$$M = \Gamma_1^{-\frac{1}{2}}\Omega_{12}\Gamma_2^{-\frac{1}{2}} \tag{15}$$

where matrix $\Gamma_i^{-\frac{1}{2}}$ $(i = 1, 2)$ is defined from the diagonal form. These singular values correspond to optimized degrees of coherence [23]. An advantage of this decomposition is that the three terms are comparable with each other since they are expressed with the same "*units*".

2.4. DPM Model and Histogram Clustering

DPM models provide a Bayesian framework for clustering problems with an unknown number of groups. DPM models may be interpreted as mixture models. The number of mixture components is a random variable and may be estimated from the data.

We model a set of observations $\{x_1, \ldots, x_n\}$ using a set of latent parameters $\{\theta_1, \ldots, \theta_n\}$. Each is drawn independently and identically from G, while each x_i has distribution $F(\cdot|\theta_i)$ parameterized by θ_i:

$$\begin{aligned} x_i|\theta_i &\sim F(\cdot|\theta_i) \\ \theta_i|G &\sim G \\ G|\alpha, G_0 &\sim DP(\alpha, G_0), \end{aligned} \tag{16}$$

where the scalar $\alpha \in \mathcal{R}_+$ is called the concentration parameter, and G_0 is a probability measure called the base measure of the process. $DP(\alpha, G_0)$ denotes the Dirichlet process parameterized by α and G_0.

Inference for DPM is usually handled by Gibbs sampling. The sampling algorithm [18, 24] for DPM is shown in Algorithm 1. From the inference process we can see, sufficient numbers of additional draws will eventually result in drawing from base measure G_0 that may generate new classes, the number of classes N_C can be regarded as a random variable. This shows that the DPM model is capable of adjusting the number of classes without switching models.

In the framework of DPM based histogram clustering, local histograms are first extracted as features. In a general mathematical sense, a histogram is a function that counts the number of observations that fall into each of the disjoint categories (known as bins). Each histogram is described by a vector $\mathbf{h}_i = (h_{i1}, \ldots, h_{iN_{bins}})$ which are non-negative integers, where N_{bins} is the number of the histogram bins. In the histogram clustering algorithm, the histogram $\mathbf{h}_1, \ldots, \mathbf{h}_n$ are input features, replacing the observations $\{x_1, \ldots, x_n\}$ discussed previously.

3. PROPOSED ALGORITHM

In this section, we present the proposed algorithm. The algorithm first calculates the Shannon entropy characteristics of the PolInSAR data and uses the three terms $\mathcal{S}_I[\Upsilon]$, $\mathcal{S}_P[\Upsilon]$ and $\mathcal{S}_\mu[\Upsilon]$ as the multichannel

Algorithm 1: DPM sampling

Initialize Generate a single cluster containing all points: $\theta_1^* \sim G_0(\theta_1^*) \prod_{i=1}^{n} F(x_i|\theta_1^*)$

Repeat

1. Generate a random permutation σ of the data indices.
2. *Assignment step.*

for $i = \sigma(0), \ldots, \sigma(n)$ **do**

a). If x_i is the only observation assigned to its cluster $k = S_i$, remove this cluster.

b). Compute the cluster probabilities $q_{i0} \propto \alpha \int_{\Omega_0} F(x_i|\theta) G_0(\theta) d\theta, q_{ik} \propto n_k^{-i} F(x_i|\theta_k^*), k = 1, 2, \ldots, N_C$.

n_k^{-i} denotes the number of samples in group k, with the additional superscript indicating the exclusion of x_i.

c). Draw a random index k according to the finite distribution $(q_{i0}, \ldots, q_{iNc})$.

d). Assignment:

if $k \in 1, \ldots, N_c$ **then** assign x_i to cluster k.

else create a new cluster for x_i.

3. *Parameter update step*: For each cluster $k = 1, \ldots, N_C$, update the cluster parameters θ_k^* given the class assignments $S_1, \ldots, S_n$ by sampling $\theta_k^* \sim G_0(\theta_k^*) \prod_{i|S_i=k}^{n} F(x_i|\theta_1^*)$

Estimate assignment model *For each point, choose the cluster it was assigned to most frequently during a given final number of iterations.*

data to extract local histograms, which are the basic inputs for the DPM-based histogram clustering procedure. AMD is applied to one polarimetric channel of the PolInSAR data. Next, pixels are divided into three canonical scattering categories according to the dominant scattering power of P_s, P_v and P_d for surface, volume and double-bounce scattering, respectively. For pixels not clearly dominated by one of these scattering mechanisms, an additional category of mixed scattering can be defined [13]; finer division of the scattering categories is discussed in [15]. For simplicity, we consider just three scattering categories here (i.e., determining the scattering categories by the maximum power among three components). The pixels in the PolInSAR image are then initially classified using scattering category labels and each is associated with its local histogram feature.

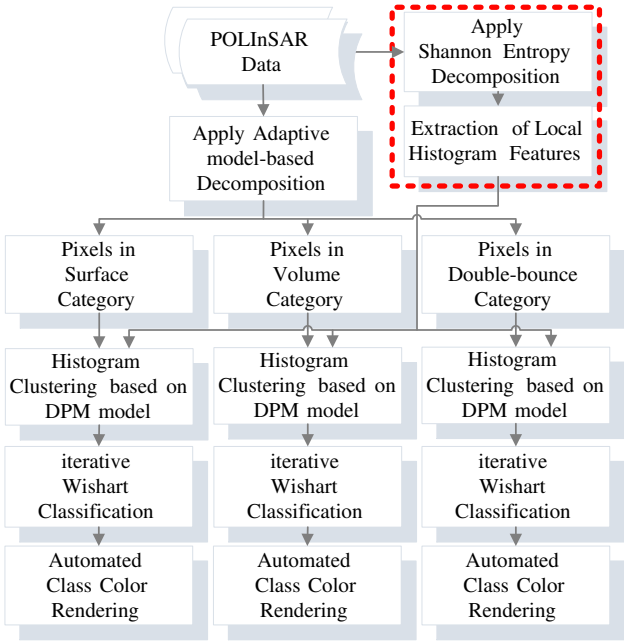

Figure 1. Flowchart of the proposed algorithm.

The scattering category label is fixed for each pixel throughout the classification process to preserve the purity of the scattering characteristics. We devised a new and effective initialization for the classes by applying histogram clustering algorithms to each of the categories. The number of classes can be evaluated simultaneously. A flowchart of this algorithm is shown in Fig. 1.

A. ***Extraction of the characteristics and initial clustering***

1) We first extract the Shannon entropy characteristics from the PolInSAR data and use the three Shannon entropy terms as multichannel input images to extract local histograms. For a given channel, histogram feature extraction is performed pixel-wise. A square histogram window is placed around each pixel and a histogram $\mathbf{h}_i$ is plotted of the values for all pixels within the window. The size of the window (and therefore the number of data value records in each histogram, N_{Counts}) and the number of histogram bins N_{bins} are kept constant for the whole image. We simply combine the histograms for the three channels to form the final histogram feature for each pixel.

2) Decompose each pixel using the AMD and compute the powers P_s, P_v and P_d. This decomposition is applied to one polarimetric channel of the PolInSAR data. Label each pixel with the dominant scattering mechanism (i.e., the maximum of the power) as surface (S), volume (V) or double-bounce (DB).

B. *Auto clustering using a histogram clustering model*

3) For each category, we perform the DPM clustering procedure using the histogram features for all pixels. The histograms $\mathbf{h}_1, \ldots, \mathbf{h}_n$ are the input features of the DPM clustering algorithm. The parameters drawn from the DP in the DPM model are the probabilities of the histogram bins. Histograms are multinomially distributed and the likelihood is chosen according to

$$\begin{aligned} F(\mathbf{h}_i|\theta_i) &= N_{Counts}! \prod_{j=1}^{N_{bins}} \frac{\theta_{ij}^{h_{ij}}}{h_{ij}} \\ &= \frac{1}{Z_M(\mathbf{h}_i)} \exp\left(\sum_{j=1}^{N_{bins}} \log(\theta_{ij})\right). \end{aligned} \tag{17}$$

The prior distribution of the parameter vectors is assumed to be a Dirichlet distribution of dimension N_{bins}, forming a conjugate pair

$$\begin{aligned} G_0(\theta_i|\beta\pi) &= \frac{\Gamma(\beta)}{\prod_{j=1}^{N_{bins}} \Gamma(\beta\pi_j)} \prod\nolimits_{j=1}^{N_{bins}} \theta_{ij}^{\beta\pi_j - 1} \\ &= \frac{1}{Z_D(\beta\pi)} \exp\left(\sum\nolimits_{j=1}^{N_{bins}} (\beta\pi_j - 1) \log(\theta_{ij})\right), \end{aligned} \tag{18}$$

where π is a N_{bins}-dimensional probability vector and β is a positive scalar. For this particular conjugate pair distribution, the corresponding formulas in Algorithm 1 become:

$$\tilde{q}_{i0} := \alpha \frac{Z_D(\mathbf{h}_i + \beta\pi)}{Z_D(\beta\pi)}; \quad \tilde{q}_{ik} := n_k^{-i} \exp\left(\sum\nolimits_j (h_{ij} \log \theta_{kj}^*)\right).$$

Class probabilities are obtained by normalization:

$$\tilde{q}_{ik} := \frac{\tilde{q}_{ik}}{\sum_{l=0}^{Nc} \tilde{q}_{il}}; \quad k = 0, \ldots, N_C. \tag{19}$$

The posterior distribution to be sampled is Dirichlet as well:

$$G_0(\theta_k^*|\beta\pi) \prod\nolimits_{i|S_i=k} F(\mathbf{x}_i|\theta_k^*) \propto G_0\left(\theta_k^*|\beta\pi + \sum\nolimits_{i|S_i=k} \mathbf{h}_i\right). \tag{20}$$

Then the pixels are divided into different classes and the number of classes N_d is determined automatically. As we insist to cluster pixels in each scattering category respectively, the resulting classes keep homogeneous in scattering and have the labels "S","V" or "DB".

C. ***Iterative K-means Wishart classification***

4) As the coherency matrix also follows a complex Wishart distribution with Υ, the 6×6 average coherency matrices from the N_d classes are computed and used as the class centers. Within each basic scattering category, all pixels are reclassified according to their Wishart distance from the class centers.
5) Iterative clustering with the Wishart classifier is applied in each scattering category. We can use the ratio of the changed labels or the number of iterations as the iteration termination criterion.

D. ***Auto color rendering***

6) After the final classification, each class is color-coded for visual evaluation of the classification results. The principle of the color coding follows the scheme of Lee et al. [13].

4. EXPERIMENTAL RESULTS

In this section, we illustrate the effectiveness of the proposed classification algorithm using E-SAR PolInSAR data from the German Aerospace Center (DLR). The E-SAR data were acquired in the L band using a repeat-pass model as part of a multi-baseline experiment in May 1998; images of 1300×1200 pixels were collected in the Oberpfaffenhofen area of Germany. The resolution is 3.00×2.20 m and the look angle spans from 25° to 60°. The average baseline across the scene is approximately 26 m and the height of the platform is 3 km. The original data were multi-look processed and filtered using a boxcar filter. The scene is composed of various agricultural areas, forests and urban zones, and buildings at the center correspond to the DLR. Fig. 2 shows the optical image and details of several typical sample areas.

Figure 3 shows characterization images for the data. Fig. 3(a) is the original image with Pauli matrix components $|S_{hh} - S_{vv}|$, $|S_{hv}|$ and $|S_{hh} + S_{vv}|$ for the three composite colors. Figs. 3(b) and (c) show the Freeman decomposition and the AMD, using $|P_d|$, $|P_v|$ and $|P_s|$ for red, green and blue respectively. The model-based decomposition methods yield similar characteristics to the Pauli-based decomposition but they provide more realistic representations. The two model-based decompositions yield similar visual characterizations, but the

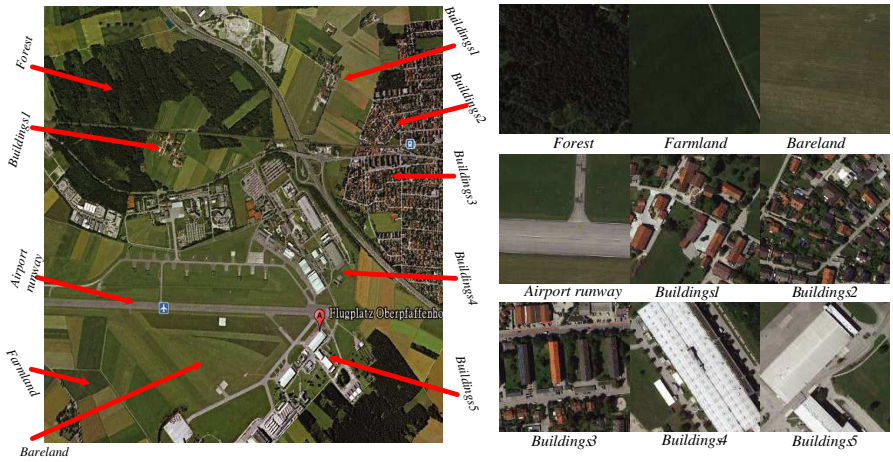

(a) (b)

Figure 2. E-SAR PolInSAR data set for Oberpfaffenhofen, Germany. (a) The corresponding optical image from Google earth®. (b) Sample areas for different scenes, including forest, farmland, bare land, airport runway, and building areas 1–5.

AMD can yield more valuable estimations for scattering areas in the vegetation canopy because of the general volume model adopted. Figs. 3(e) and (f) show the intensity, polarimetric and interferometric contributions to Shannon entropy. It is evident that the three entropy contributions reveal different properties of the different zones and yield good discrimination. Because the three terms are comparable with each other, we use them as multi-channel data for local histogram feature extraction in DPM model-based histogram clustering. In our experiments the size of the histogram window is five and hence N_{Counts} is 25. We set N_{bins} to 4 for each histogram in each data channel. We cascade the histograms for each pixel for simplicity.

After the initial segmentation, the pixels are divided into three categories labeled as S, V and DB. The histogram clustering algorithm is applied to each of the categories, classes are initialized and we obtain the cluster numbers. The estimated number of classes is 12, comprising five for the surface, three for the volume and four for the double-bounce scattering categories. The histogram clustering algorithm is iterated 200 times and the results of the last 100 iterates are used for mode estimation. Iterative Wishart classification is then performed to refine the result. The color rendering scheme uses brown colors for surface, green colors for volume, and red colors for double-bounce scattering classes. The final classification result is shown in Fig. 4(b). Since the

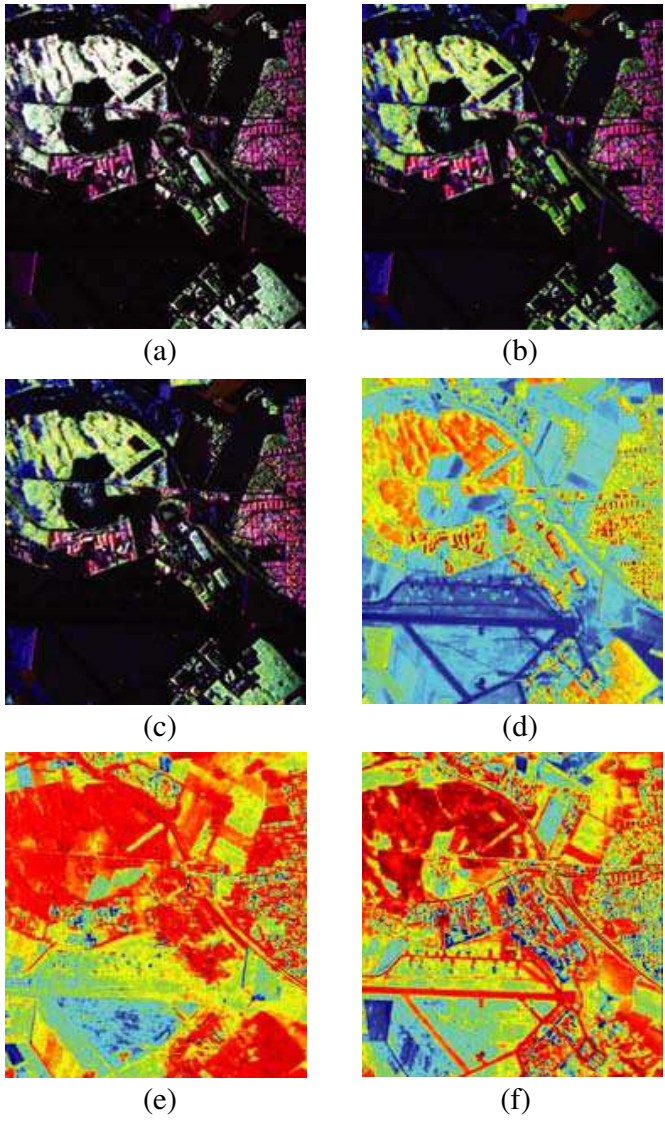

Figure 3. Characterization images for the PolInSAR data. (a) Image using Pauli matrix components $|S_{hh}-S_{vv}|$, $|S_{hv}|$ and $|S_{hh}+S_{vv}|$ for red, green and blue, respectively. (b) Freeman decomposition using $|P_d|$, $|P_v|$ and $|P_s|$ for the three RGB channels. (c) The AMD. (d) Intensity. (e) Polarimetric and (f) interferometric contributions to the Shannon entropy.

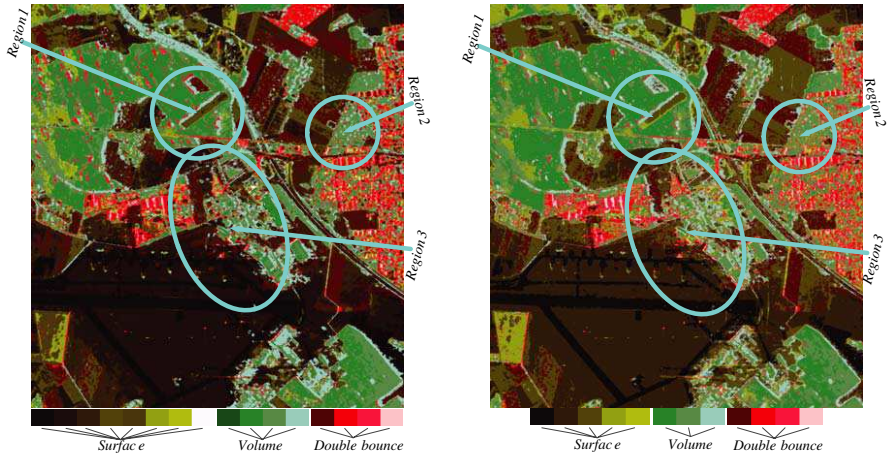

(a) Lee's algorithm (b) Proposed method

Figure 4. Classification maps and automated color rendering for classes. (a) PolSAR classification results according to (a) Lee's algorithm and (b) the proposed method. For Lee's method, we manually specified the number of classes as eight, four and four for surface, volume and double-bounce scattering categories, respectively. For the proposed method, the corresponding numbers generated automatically were five, three and four.

scattering-preserving classification algorithm proposed by Lee et al. [13] has better stability in convergence and when the number of classes is selected elaborately, it could achieve quite well results, we consider it as a benchmark for comparison. Fig. 4(a) shows the results obtained by Lee's method with eight S, four V and four DB classes.

Comparison of the two color-coded images in Fig. 4 reveals that the two algorithms yield very similar and consistent classification results. The forest and vegetation areas are well classified and show different scattering properties compared to farmland and other areas with low-growing plants. The surface scattering classes show great distinction in separating airport runways, grassland, bare land and plowed fields. We can observe several meta reflectors coded with bright colors in the triangle above the runway. The DB classes clearly show the street patterns associated with building blocks and the edges of buildings facing the radar. Since the number of classes is specified manually in Lee's method, the classification results suggest that the class numbers generated by our algorithm are reasonable and acceptable.

We can still observe some differences in results between the two methods. Since the number of classes specified in Lee's method is greater, the method yields more fine details. For example, in Fig. 4(a) the meta reflectors have more precise shapes and edges of buildings are clearer. However, our method achieves better results in homogeneous regions. In the top left corner, Lee's method segments the ground between two large vegetation areas into several trivial blocks, while our method classifies them as a whole. Similar results are evident for the plowed fields in the bottom left corner and flat areas outside the town. To examine the results of the two algorithms in detail, we magnified the three highlighted areas, as shown in Fig. 5, where region 1 is a forest area, region 2 covers a corner of the town and region 3 shows the DLR buildings and a corner of the airport. For the forest area, Lee's method classifies more pixels as DB scattering, while our method misclassifies the glade as volume scattering. For the urban area, some of buildings are misclassified as volume scattering by the two methods because they are not aligned facing the radar. For region 3, buildings with large roofs are all misclassified as volume scattering, and we can see the hangars along the runway clearly. To better illustrate the performance of the two algorithms, we quantitatively evaluated these areas using the purity (the higher the better) and entropy gain (the lower the better) defined in [25]. The two measures of homogeneity are defined as follows:

$$\begin{aligned} Purity &= \sum_{r=1}^{k} \frac{1}{n} \max_i \left(n_r^i\right) \\ Entropy &= \sum_{r=1}^{k} \frac{n_r}{n} \left(-\frac{1}{\log\ q} \sum_{i=1}^{q} \frac{n_r^i}{n_r} \log \frac{n_r^i}{n_r} \right), \end{aligned} \tag{21}$$

where q is the number of classes, k the number of clusters obtained, n_r the size of cluster r, and n_r^i the number of data points in class i in cluster r. The results in Table 1 show that the two algorithms achieve very similar scores, confirming their comparative performance.

Most of the misclassifications occur in urban areas because of variations in building type and orientation, which can induce different

Table 1. Purity and entropy of the test areas.

Images	Region 1		Region 2		Region 3	
Algorithm	Purity	Entropy	Purity	Entropy	Purity	Entropy
Lee's method	0.829	0.321	0.650	0.489	0.616	0.596
Proposed method	0.821	0.321	0.643	0.489	0.620	0.583

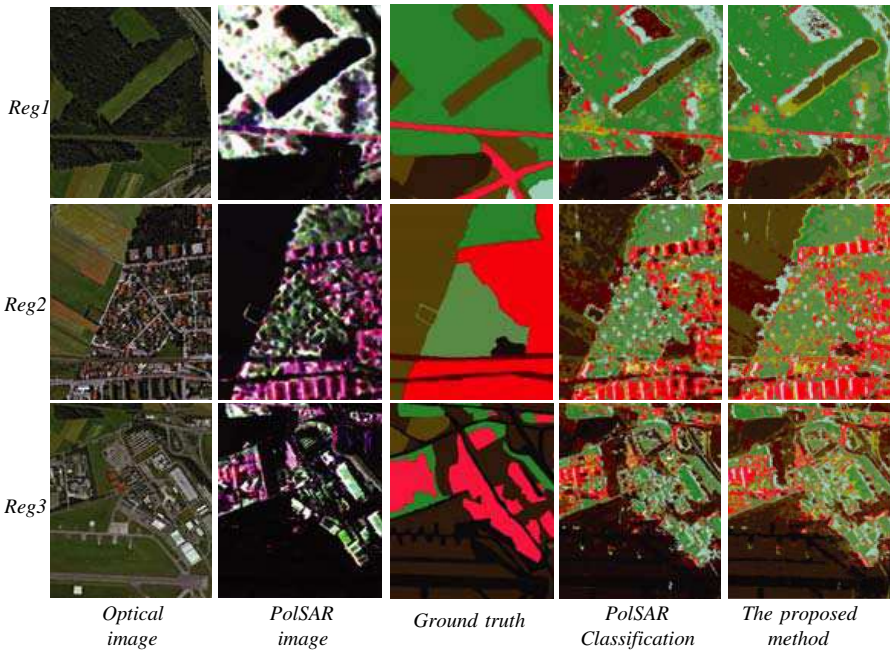

Figure 5. Details of the classification results for the three regions highlighted in Fig. 4.

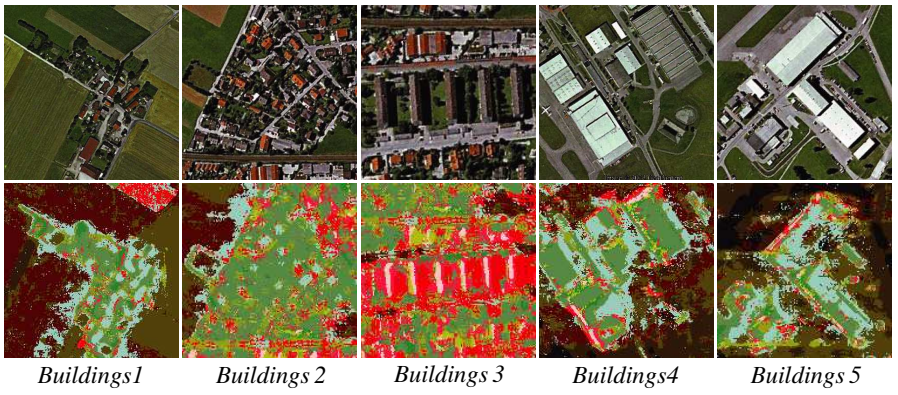

Figure 6. Classification results obtained using the proposed algorithm for different building areas.

scattering responses. Fig. 6 shows optical image and classification results for five building regions marked in Fig. 2. Although these areas all consist of buildings, the classification results are quite different. Regions 1 and 2 are classified as volume scattering because the buildings do not face the radar, so they do not induce DB responses. Region 3 is correctly classified as DB scattering because the buildings face the radar. Regions 4 and 5 are classified as volume scattering because they have large rough roofs. It should be noted that although the building areas are misclassified as volume scattering, they are not classified to the same class as forest areas, which are colored darker green. The results for regions 4 and 5 show that as the resolution increases, we should pay more attention to the structure information in the classification algorithm.

5. CONCLUSION AND DISCUSSION

We proposed a data-driven unsupervised classification algorithm for PolInSAR data. The algorithm divides pixels into three canonical scattering categories by applying AMD, which overcomes the flaw of Freeman decomposition. We utilized Shannon entropy characteristics of the PolInSAR data to extract local histogram features. This characterization provides a suitable way of describing intensity, polarimetric and interferometric information in comparable expressions. To each of three basic scattering categories we applied a histogram clustering algorithm based on the DPM model. This method provides a Bayesian framework for clustering problems with an unknown number of groups. After determining the number of classes and class centers, the iterative Wishart classifier was applied to refine the classification result. Our algorithm is automatic and data-driven, and shows comparative performance to the algorithm proposed by Lee et al. [13], which needs artificial pre-assigned number of classes.

The main purpose of the proposed algorithm is to classify data from the point of scattering mechanism, so we only use the Shannon entropy characterization of the PolInSAR data to extract local histogram features for DPM model-based histogram clustering, and interferometric PolInSAR information is not fully used. Further analysis of the classification result combined with the interferometric information will be discussed in future work. In our framework we used the Shannon entropy characterization to extract local histogram features, but this characterization is not the only choice and may be replaced by a more suitable one.

ACKNOWLEDGMENT

The research was supported in part by the National Key Basic Research and Development Program of China under Contract 2013CB733404 and the National Natural Sciences Foundation of China grants (NSFC) 61271401.

REFERENCES

1. Kong, J. A., S. H. Yueh, H. H. Lim, R. T. Shin, and J. J. Van Zyl, "Classification of earth terrain using polarimetric synthetic aperture radar images," *Progress In Electromagnetics Research*, Vol. 3, 327–370, 1990.
2. Lee, J., M. Grunes, and R. Kwok, "Classification of multi-look polarimetric SAR imagery based on complex wishart distribution," *International Journal of Remote Sensing*, Vol. 15, No. 11, 2299–2311, 1994.
3. Ferro-Famil, L. and E. Pottier, "Dual frequency polarimetric SAR data classification and analysis," *Progress In Electromagnetics Research*, Vol. 31, 247–272, 2001.
4. Jin, Y.-Q., "Polarimetric scattering modeling and information retrieval of SAR remote sensing — A review of FDU work," *Progress In Electromagnetics Research*, Vol. 104, 333–384, 2010.
5. Goodman, N., "Statistical analysis based on a certain multivariate complex gaussian distribution (an introduction)," *Annals of Mathematical Statistics*, 152–177, 1963.
6. Cloude, S. and E. Pottier, "An entropy based classification scheme for land applications of polarimetric SAR," *IEEE Transactions on Geoscience and Remote Sensing*, Vol. 35, No. 1, 68–78, 1997.
7. Lee, J., M. Grunes, T. Ainsworth, L. Du, D. Schuler, and S. Cloude, "Unsupervised classification using polarimetric decomposition and the complex wishart classifier," *IEEE Transactions on Geoscience and Remote Sensing*, Vol. 37, No. 5, 2249–2258, 1999.
8. Pottier, E. and J. Lee, "Unsupervised classification scheme of polsar images based on the complex wishart distribution and the H/A/alpha polarimetric decomposition theorem (polarimetric sar)," *EUSAR 2000*, 265–268, 2000.
9. Van Zyl, J., "Unsupervised classification of scattering behavior using radar polarimetry data," *IEEE Transactions on Geoscience and Remote Sensing*, Vol. 27, No. 1, 36–45, 1989.
10. Ferro-Famil, L., E. Pottier, and J. Lee, "Unsupervised

classification of natural scenes from polarimetric interferometric SAR data," *Frontiers of Remote Sensing Information Processing*, 105, 2003.

11. Ferro-Famil, L., E. Pottier, H. Skriver, P. Lumsdon, R. Moshammer, and K. Papathanassiou, "Forest mapping and classification using L-band polinSAR data," *ESA Special Publication*, Vol. 586, 9, 2005.
12. Cloude, S. and E. Pottier, "A review of target decomposition theorems in radar polarimetry," *IEEE Transactions on Geoscience and Remote Sensing*, Vol. 34, No. 2, 498–518, 1996.
13. Lee, J., M. Grunes, E. Pottier, and L. Ferro-Famil, "Unsupervised terrain classification preserving polarimetric scattering characteristics," *IEEE Transactions on Geoscience and Remote Sensing*, Vol. 42, No. 4, 722–731, 2004.
14. Freeman, A. and S. Durden, "A three-component scattering model for polarimetric SAR data," *IEEE Transactions on Geoscience and Remote Sensing*, Vol. 36, No. 3, 963–973, 1998.
15. Yang, W., T. Zou, H. Sun, and X. Xu, "Improved unsupervised classification based on freeman-durden polarimetric decomposition," *EUSAR 2008, 7th European Conference on Synthetic Aperture Radar*, 1–4, VDE, 2008.
16. Van Zyl, J., M. Arii, and Y. Kim, "Model-based decomposition of polarimetric SAR covariance matrices constrained for nonnegative eigenvalues," *IEEE Transactions on Geoscience and Remote Sensing*, Vol. 49, No. 9, 3452–3459, 2011.
17. Arii, M., J. Van Zyl, and Y. Kim, "Adaptive model-based decomposition of polarimetric SAR covariance matrices," *IEEE Transactions on Geoscience and Remote Sensing*, Vol. 49, No. 3, 1104–1113, 2011.
18. Orbanz, P. and J. Buhmann, "Nonparametric Bayesian image segmentation," *International Journal of Computer Vision*, Vol. 77, No. 1, 25–45, 2008.
19. Morio, J., P. Réfrégier, F. Goudail, P. Dubois-Fernandez, and X. Dupuis, "Information theory-based approach for contrast analysis in polarimetric and/or interferometric SAR images," *IEEE Transactions on Geoscience and Remote Sensing*, Vol. 46, No. 8, 2185–2196, 2008.
20. Morio, J., P. Réfrégier, F. Goudail, P. Dubois-Fernandez, and X. Dupuis, "A characterization of shannon entropy and Bhattacharyya measure of contrast in polarimetric and interferometric SAR image," *Proceedings of the IEEE*, Vol. 97, No. 6, 1097–1108, 2009.

21. Van Zyl, J., "Application of cloude's target decomposition theorem to polarimetric imaging radar data," *Proc. SPIE 1748, Radar Polarimetry*, 184–191, International Society for Optics and Photonics, 1993.
22. Réfrégier, P., F. Goudail, P. Chavel, and A. Friberg, "Entropy of partially polarized light and application to statistical processing techniques," *Journal of the Optical Society of America A (JOSA A)*, Vol. 21, No. 11, 2124–2134, 2004.
23. Cloude, S. and K. Papathanassiou, "Polarimetric SAR interferometry," *IEEE Transactions on Geoscience and Remote Sensing*, Vol. 36, No. 5, 1551–1565, 1998.
24. Neal, R., "Markov chain sampling methods for dirichlet process mixture models," *Journal of Computational and Graphical Statistics*, Vol. 9, No. 2, 249–265, 2000.
25. Rosenberg, A. and J. Hirschberg, "V-measure: A conditional entropy-based external cluster evaluation measure," *Proceedings of the 2007 Joint Conference on Empirical Methods in Natural Language Processing and Computational Natural Language Learning (EMNLP-CoNLL)*, Vol. 410, 420, 2007.